Geophysical Research Letters

RESEARCH LETTER
10.1029/2018GL079887

Key Points:
- Hydrogen isotope compositions of ancient meteoric waters constrain past elevations across the North American Cordillera of the western US
- Paleoelevation data indicate that a high plateau existed during the Eocene across Utah and eastern Nevada prior to Farallon slab rollback
- Rollback processes generated additional uplift of 400-600 m, far less than previous estimates, followed by orogenic collapse

Supporting Information:
- Supporting Information S1
- Figure S1
- Table S1
- Table S2

Correspondence to:
E. J. Cassel,
ecassel@uidaho.edu

Citation:
Cassel, E. J., Smith, M. E., & Jicha, B. R. (2018). The impact of slab rollback on Earth's surface: Uplift and extension in the hinterland of the North American Cordillera. *Geophysical Research Letters*, *45*. https://doi.org/10.1029/2018GL079887

Received 3 AUG 2018
Accepted 17 SEP 2018
Accepted article online 21 SEP 2018

The Impact of Slab Rollback on Earth's Surface: Uplift and Extension in the Hinterland of the North American Cordillera

Elizabeth J. Cassel[1], M. Elliot Smith[2], and Brian R. Jicha[3]

[1]Department of Geological Sciences, University of Idaho, Moscow, ID, USA, [2]School of Earth Sciences and Environmental Sustainability, Northern Arizona University, Flagstaff, AZ, USA, [3]Department of Geoscience, University of Wisconsin-Madison, Madison, WI, USA

Abstract Slab rollback processes alter the intraplate force balance and buoyancy of the overriding plate, driving surface uplift or extension. From ca. 55–24 Ma, Farallon slab rollback produced migrating volcanism and sedimentation across the western United States as stress on the North American plate transitioned from subduction-driven compression to widespread extension. Hypotheses regarding rollback-driven surface deformation differ widely in timing and magnitude. Here we combine hydrogen isotope ratios with high-resolution geochronology to show that a high-elevation plateau extended westward from the Sevier-Laramide fold-thrust belt across Utah and eastern Nevada prior to slab rollback. Quantitative paleoelevation estimates show that this plateau had obtained over 80% of peak paleoelevations by middle Eocene. Slab rollback, heating, and lithospheric delamination generated 400–600 m of Oligocene surface uplift. Concurrent extension limited overall uplift and rollback-induced mantle flow likely contributed to the propagation of upper crustal extension that formed the Basin and Range province.

Plain Language Summary Changes in surface elevations are critical to understanding the formation and evolution of mountains and basins across ancient landscapes. Slab rollback—retreat and steepening of the downgoing tectonic plate during subduction—can transform Earth's surface by altering the stresses on the overriding plate. By measuring the ratios of hydrogen isotopes in ancient rainwater, preserved for millions of years in volcanic ash, we can estimate past elevations. Here we measure past elevations across the Basin and Range province of Utah and Nevada to reconstruct topography before and during slab rollback. Results show that a high elevation plateau extended westward from the western edge of the Rocky Mountains across Utah and eastern Nevada prior to slab rollback. Slab rollback generated a short-lived interval of 400–600 m of surface uplift, much less than has been previously estimated. Instead, subsequent processes resulting from rollback likely contributed to collapse of the high plateau and the widespread extensional faulting that created the characteristic topography of the modern Basin and Range province.

1. Introduction

Tectonic plate boundary forces, surface processes, and mantle flow all apply stress that deforms overriding plates during subduction and propagates across broad regions to alter surface topography. Past changes in surface elevation thus provide a unique tool to reconstruct the timing and relative contributions of these forces, but until recently, measuring past elevations at the scale and resolution of entire mountain belts has proven difficult. Slab rollback, where a subducting slab migrates in the direction opposite to its overall plate motion, may drive surface uplift in the overriding plate through isostatic adjustment to heating, unloading, and lithospheric delamination or subsidence through loading, shear, and extension driven by mantle flow or gravitational collapse (Brun et al., 2016; Chen et al., 2016; DeCelles & Graham, 2015; Humphreys, 2009; Porter et al., 2017; Smith et al., 2017; Sternai et al., 2014). Numerical models have shown that basal shear and toroidal mantle flow related to slab rollback contribute to both vertical and subhorizontal surface strain, control the locations and kinematics of extension, and alter the mechanical properties of the overlying lithosphere (Brun et al., 2016; Chen et al., 2016; Sternai et al., 2014). But the interactions and effects of magmatism, heating, delamination, and mantle flow during slab rollback are poorly constrained for past rollback events, particularly in the North American Cordilleran hinterland where rollback and multiphase extension appear to overlap in space and time (Best et al., 2016; Cassel et al., 2014; Chamberlain et al., 2012; Constenius, 1996;

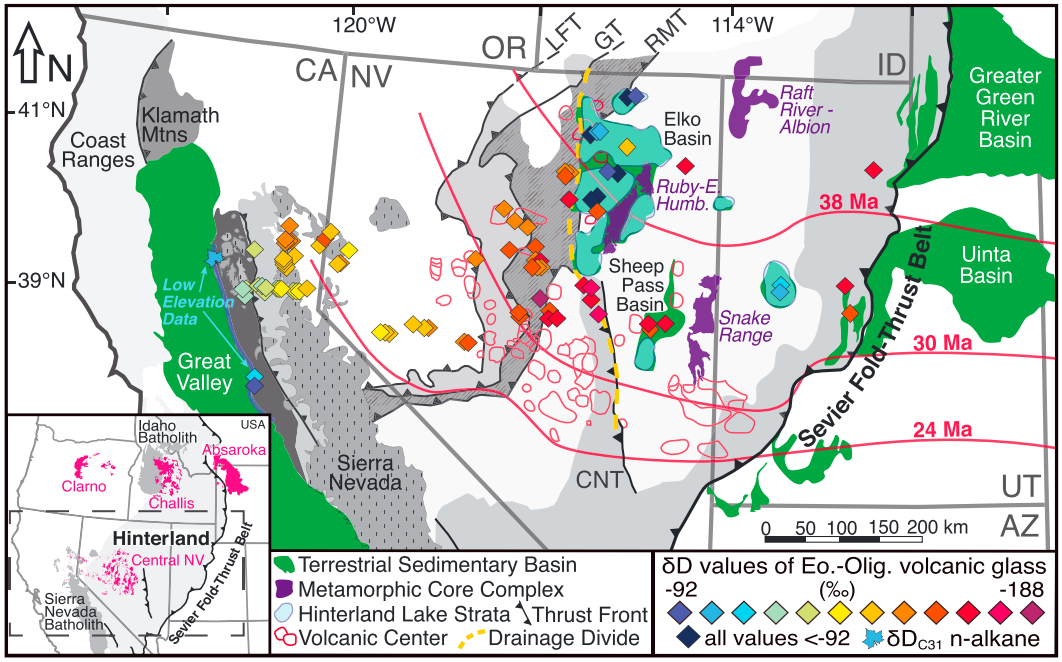

Figure 1. Geologic map of the central North American Cordilleran hinterland. (inset) Hinterland in light gray between the Sevier fold-thrust belt and the Mesozoic volcanic arc (in dark gray); Cenozoic volcanics in pink. (main) Basement terranes in grayscale, Paleogene: lake strata in light blue, sedimentary basins in green, core complexes in purple, and volcanic centers outlined in red. Thick red lines show rollback magmatism (Best et al., 2016). Glass samples shaded by δD value (diamonds). δD values of all ages decrease from the paleoshoreline (blue line) to the paleodrainage divide (yellow-dashed line) by ~100‰, except for samples hydrated by lacustrine waters. All δD values located east of the paleodrainage divide, up to 350 km, are equal within ±3‰ uncertainty. Pre-Sevier thrust fronts: Luning-Fencemaker (LFT), Golconda (GT), Roberts Mountain (RMT), and Central Nevada thrust (CNT).

DeCelles, 2004; Henry et al., 2012; Wells et al., 2012). Most hypotheses closely link magmatism and deformation, but estimates of rollback-driven deformation range from 2.5 to 4 km of surface uplift from asthenospheric heating to the initiation of rapid metamorphic core complex extension facilitating gravitational collapse, either triggered by or causing magmatism (e.g., Armstrong & Ward, 1991; Chamberlain et al., 2012; M. Liu, 2001). Although researchers have made major advances on the exhumation mechanics and preextensional elevations of core complexes (Bendick & Baldwin, 2009; Gébelin et al., 2012; Mulch et al., 2007; Rey et al., 2009b; Whitney et al., 2013), the timing, topography, and dynamics of orogenic collapse remain controversial (e.g., Colgan & Henry, 2009; Konstantinou et al., 2012; Methner et al., 2015; Rey et al., 2009a).

Farallon plate subduction drove crustal thickening in the North American Cordillera through retroarc fold-thrust belts, lithospheric underthrusting, and arc magmatism starting in the Jurassic (DeCelles, 2004; DeCelles & Graham, 2015). Arc magmatism ended at 80 Ma in the Sierra Nevada, and deformation migrated eastward due to shallowing of the slab subduction angle, initiating Laramide basement-involved faulting, shortening, and basin formation in the foreland that continued to into the early Eocene (Copeland et al., 2017; Heller & Liu, 2016). Magmatism then resumed at the furthest extents of the region of Laramide deformation and migrated southwest across previously deformed regions from the Challis and Absaroka volcanic fields at ca. 49 Ma to central Nevada by ca. 30 Ma (Figure 1; Best et al., 2016; Coney & Harms, 1984; Dickinson, 2009; Smith et al., 2014). Researchers attribute this progression of volcanism, and contrasts in modern upper mantle seismic velocities, to asthenospheric mantle heating of hydrated continental lithosphere following Farallon slab rollback (Dickinson, 2009; Humphreys, 2009).

There are a range of hypotheses for the evolution of hinterland topography prior to and during Farallon slab rollback, including Late Cretaceous or Eocene orogenic collapse, relative stability until Miocene collapse, or Eocene uplift. Thrust belt structural analysis and drainage reconstructions suggest that crustal shortening had produced thickened crust and high paleoelevations by Late Cretaceous across the hinterland—

sometimes termed *the Nevadaplano* in reference to the Andean Altiplano (Axelrod, 1997; Best et al., 2016; Cassel et al., 2014; DeCelles, 2004; Henry et al., 2012; Long, 2012; Mulch et al., 2006). Previous workers have interpreted thermobarometric, thermochronologic, and localized fault data as signals of synconvergent extension initiating in the Late Cretaceous due to gravitational spreading (Druschke et al., 2009; Hodges & Walker, 1992; Long et al., 2015; Wells et al., 2012). Others have used thermochronologic, stratigraphic, and isotopic data from metamorphic core complexes and terrestrial sedimentary basins to show extensional exhumation beginning by 55 Ma in British Columbia and progressing southward to Nevada by ca. 40 Ma, roughly synchronous with rollback magmatism (Figure 1), suggesting that supracrustal extension and gravitational collapse of the hinterland began in the Eocene (Constenius, 1996; Dickinson, 2009; Evans et al., 2015; Gébelin et al., 2015; Sonder & Jones, 1999). Still other workers suggest that drainage reconstructions, chronostratigraphy, and low-temperature thermochronology show only minor extension until the Miocene (Colgan & Henry, 2009; Konstantinou et al., 2012; Lund Snee et al., 2016).

Despite these records of extension and gravitational spreading, contemporaneous paleoaltimetry data thus far show only high or increasing hinterland elevations in the Paleogene (e.g., Mulch et al., 2006, 2007; Wolfe et al., 1998). Based on shifts in stable isotope ratios from hinterland basin strata, researchers have interpreted 2.5 to 4 km of migrating surface uplift, driven by the southward advance of rollback magmatism and delamination of mantle lithosphere, that generated a high elevation, high relief Eocene landscape (Chamberlain et al., 2012; Feng et al., 2013; Mix et al., 2011). Multiple Paleogene paleoelevation profiles from western and central Nevada show large decreases in hydrogen isotope values eastward across the hinterland, indicating relatively stable high elevations (2.6–3.5 km) across Nevada from 37 to 24 Ma (Cassel et al., 2014), after the initiation of core complex exhumation in the region (Dallmeyer et al., 1986; Evans et al., 2015; McGrew & Snee, 1994). To isolate the surface effects of slab rollback, we use widespread ignimbrites and ash fall tuffs deposited both before and during slab rollback that are interbedded with hinterland sedimentary strata and age-correlative units from known low paleoelevations (Figure 1; Cassel et al., 2014; Smith et al., 2017). Here we present new hydrogen isotope ratios in volcanic glass (δD_{glass}) and sanidine $^{40}Ar/^{39}Ar$ age data that, combined with recently published paleoclimate data, quantify absolute elevations before and after slab rollback.

2. Methods to Measure Paleoelevations

In many mountain belts, elevation exerts a primary control on the δD value of precipitation (Dansgaard, 1964). As air masses lift over topography, liquid water condenses due to adiabatic cooling (Craig, 1961; Dansgaard, 1964). At isotopic equilibrium, liquid water has higher D/H ratios than coexisting water vapor, so successive precipitation events lead to progressive Deuterium depletion with elevation (Dansgaard, 1964; Rowley, 2007). After deposition, volcanic glass hydrates with meteoric water over 10^3 to 10^4 years via diffusion and exchange with mobile cations (Cassel & Breecker, 2017). Silicate glasses are chemically durable and demonstrate substantial decreases in alteration rates on long time scales due to the formation of a nanoporous, high-density, silica-rich layer near the glass exterior (Gin et al., 2015). This layer resists subsequent hydration or isotopic exchange, acting to preserve paleo-meteoric water δD values on geologic timescales (Cassel & Breecker, 2017). Individual tuffaceous units are commonly widespread and contain dateable sanidine phenocrysts (Smith et al., 2017). Unit ages and δD_{glass} values can be used to construct spatially extensive paleoelevation profiles for precise time intervals (Cassel et al., 2014).

2.1. Volcanic Glass δD Values

Pure volcanic glass separates were prepared following the methods presented in Cassel and Breecker (2017). Hydrogen isotope ratios were measured by high temperature thermal combustion and continuous-flow gas mass spectrometry on a Thermo Electron TC-EA coupled to a Thermo MAT253 isotope ratio mass spectrometer in the Light Stable Isotope Lab at The University of Texas at Austin. Three to four milligrams of acid-abraded, density-isolated 70–150-μm glass shards were wrapped in silver foil, dried under vacuum at 70 °C for at least 24 hr, and then loaded into a zero-blank auto sampler and immediately flushed with dry He gas (see also supporting information S1). Three to six repeat analyses were run on each glass separate to ensure analytical reproducibility. Isotope data have been corrected for drift over time and offset from certified international reference standard values. At least three internationally referenced standard materials and one in-house working standard were repeatedly analyzed throughout all sample runs. Based on analyses of IBS-CH7 (foil) and IBS-22 (oil) standards, precision for hydrogen isotope ratios was determined to be 2‰.

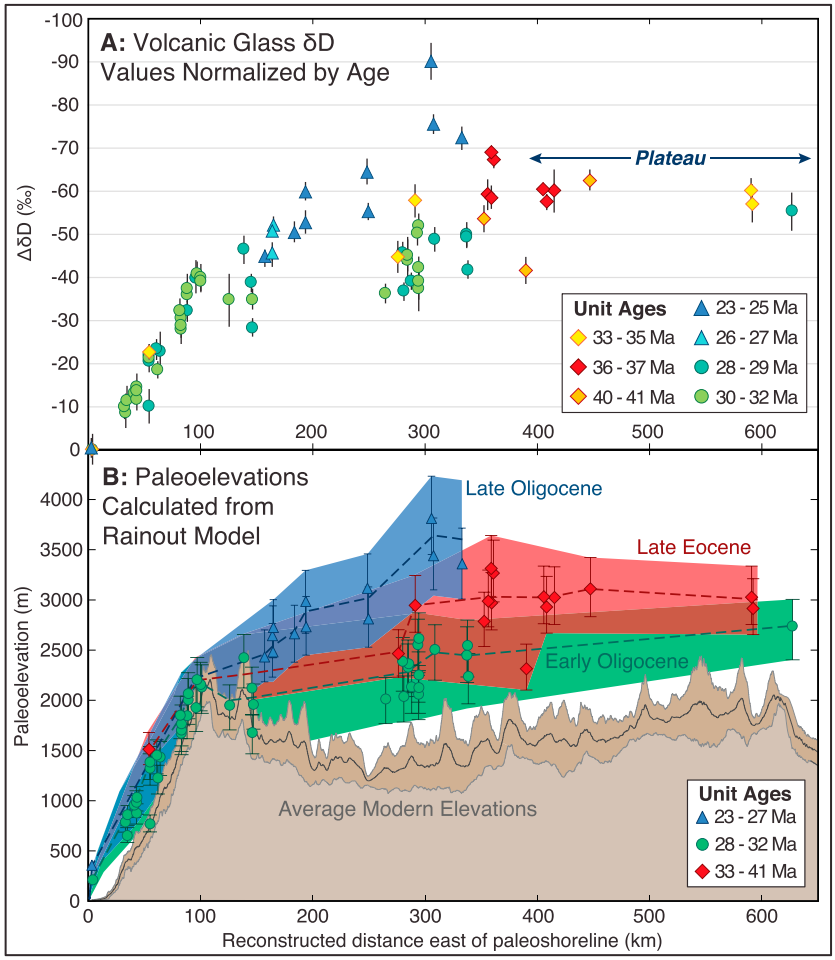

Figure 2. $\Delta\delta D_{glass}$ values and rainout model results plotted versus reconstructed distance from the Paleogene shoreline (Figure 1); error bars represent ±2σ uncertainty. (a) $\Delta\delta D_{glass}$ values normalized to low elevation datum and grouped based on $^{40}Ar/^{39}Ar$ radiometric age from each sample. Note reverse *y* axis. (b) Paleoelevations as calculated by the rainout model, with profiles (dashed lines) following mean square weighted deviate of elevations. Bars include propagated analytical error and uncertainty in initial temperature. Average modern elevations ±1σ from swath across sampling area.

To account for global changes in vapor source isotopic composition over time, we compare δD_{glass} values to a low elevation datum for each time period ($\Delta\delta D$; Cassel et al., 2014). $\Delta\delta D_{glass}$ data are plotted versus distance from the Paleogene shoreline (Figure 2a), reconstructed to remove later extension (Colgan & Henry, 2009; Henry et al., 2012). Low elevation data points were measured for the Oligocene from two newly dated tuffs overlying Eocene marine sedimentary rocks (Table 1). The Eocene datum was calculated based on an *n*-alkane δD_{C31} value sampled at 5 km from the Eocene shoreline (Hren et al., 2010), converted to its equivalent δD_{glass} value (Friedman et al., 1993; Stauffer, 2017; Xia et al., 2008; Table S1).

2.2. $^{40}Ar/^{39}Ar$ Radioisotopic Dating

δD_{glass} values are grouped based on new $^{40}Ar/^{39}Ar$ radioisotopic ages (Table 1). Sanidine phenocrysts were separated via crushing, leaching in dilute HCl and HF, and hand-picking under refractive index oils. Sanidine crystals were irradiated together with Fish Canyon tuff sanidine in the TRIGA reactor at Oregon State University in cadmium shielding. Single sanidine crystals from nine units were fused using a 25W CO_2 laser and analyzed for Ar isotopic composition using a MAP 215-50 spectrometer, and in one case, smaller sanidine were analyzed using a Noblesse multicollector mass spectrometer (Jicha et al., 2016; Table S2). Weighted mean ages were calculated using the 28.201-Ma age for Fish Canyon tuff sanidine (Kuiper et al., 2008) with fully propagated uncertainties, which incorporate decay constant, K isotopic composition, and intercalibration uncertainties (Lee et al., 2006; Min et al., 2000).

Table 1
Glass δD Value and Single-Crystal Sanidine $^{40}Ar/^{39}Ar$ Age Pairs From Hinterland Plateau Ash Beds and Low Elevation Data (VS)

Sample	Latitude (°N)	Longitude (°W)	Glass δD value (‰)	2σ	Water content (wt %)	Single sanidine analyses	Age (Ma)	2σ analytical only	2σ full	MSWD
08122VS	38.206	120.838	**−95.1**	*± 2.3*	4.03	15 of 17	**22.98**	± 0.14	*± 0.16*	0.92
08123VS	38.166	120.859	**−112.4**	*± 3.6*	3.23	14 of 18	**30.27**	± 0.23	*± 0.25*	0.62
12154NC	41.025	114.544	**−168.4**	*± 2.4*	2.98	20 of 20	**40.50**	± 0.06	*± 0.26*	1.24
14001DV	39.663	112.042	**−166.1**	*± 2.7*	3.47	9 of 20	**35.00**	± 0.19	*± 0.22*	0.73
14002DV	39.663	112.042	—	—	—	6 of 12	**27.562**	± 0.036	*± 0.095*	1.14
14009CH	39.361	111.939	**−163.0**	*± 1.8*	3.19	16 of 16	**34.76**	± 0.20	*± 0.23*	0.87
14011DL[a]	39.655	113.034	**−105.4**[a]	*± 5.8*	1.57	16 of 16	**34.47**	± 0.26	*± 0.28*	0.82
14013JY[a]	39.575	113.062	**−114.1**[a]	*± 8.9*	0.20	16 of 17	**35.30**	± 0.14	*± 0.18*	0.75
14016EL	39.219	114.906	**−166.2**	*± 2.7*	3.02	18 of 18	**36.83**	± 0.17	*± 0.21*	0.52
14019SW	39.143	114.879	**−163.5**	*± 4.4*	4.03	15 of 15	**36.57**	± 0.20	*± 0.23*	0.42
14020CL	39.202	114.687	**−165.9**	*± 1.7*	3.53	18 of 19	**36.34**	± 0.17	*± 0.21*	0.97
15056NC	40.989	111.676	**−167.7**	*± 4.4*	5.92	18 of 19	**36.34**	± 0.17	*± 0.21*	0.97

Note. Dates relative to 28.201 Ma for the Fish Canyon sanidine standard; interpreted weighted mean ages shown. δD values are reported relative to SMOW. Italics denote full uncertainties. Bold emphasis here denotes the columns of actual value age pairs. MSWD = mean square weighted deviate.
[a]Sampled from a tuff interbedded with lacustrine strata.

2.3. Paleoelevation Model

Paleoelevations across the Cordilleran hinterland were calculated from $\Delta\delta D_{glass}$ values for each time interval using a thermodynamic air mass lifting Rayleigh condensation (rainout) model (Rowley, 2007), validated using local modern meteoric water ΔδD values (Cassel et al., 2014). The model calculates the elevation change needed to generate observed ΔδD values using initial temperature, relative humidity, and distance from vapor source as input variables, based on progressive condensation as a humid air mass rises and cools adiabatically in an open system. Both the equilibrium fractionation factors between vapor and liquid and vapor and ice for subfreezing temperatures are dependent on temperature in the model (Rowley, 2007). The model is most sensitive to initial temperature, so revised initial conditions from recent data have greatly limited uncertainty in model results in comparison to previous work. Time-specific simulations account for global climate changes for Eocene and Oligocene datasets based on paleotemperature and pCO_2 proxies from terrestrial and marine records (Axelrod, 1997; Beerling & Royer, 2011; Doria et al., 2011; Feng et al., 2016; Hren et al., 2010; Z. Liu et al., 2009; Mix et al., 2016; Pearson et al., 2009; Sheldon et al., 2016; Wolfe et al., 1998). Initial mean annual temperature increases from modern of 6 °C (33–41 Ma), 4.4 °C (28–32 Ma), and 4.0 °C (27–23 Ma) are shown in Figure 2b; error bars include propagated temperature uncertainty of ±2 °C and analytical uncertainties. A relative humidity initial value of 100% was used for all time intervals as this is the most common value to result in rain in the modern Sierra Nevada. Reducing the value to 90% results in a $<$ 3% decrease in maximum paleoelevations. Latent heat, saturation vapor pressure, and air mass mixing vary with initial temperature in the model, and isotopic lapse rates decrease as temperature increases (Rowley, 2007). The model is validated using modern ΔδD values of water samples collected across California (Friedman et al., 2002; Ingraham & Taylor, 1991; Kendall & Coplen, 2001), and calculated elevations are comparable to those measured (Cassel et al., 2014). Additionally, previous global climate model studies of western North America show Pacific-sourced moisture dominated throughout the Eocene and Oligocene in the study region (Feng et al., 2016, 2013). Increased vapor subsidence over orogens due to higher pCO_2 in the Eocene and early Oligocene is represented by the upper range of elevation estimates (Poulsen & Jeffery, 2011).

3. Paleoelevations During Slab Rollback

$\Delta\delta D_{glass}$ values consistently decrease eastward to the paleodrainage divide at all time intervals, which migrated westward over time from 350- to 310-km reconstructed distance (Figures 1 and 2). East of the divide, $\Delta\delta D_{glass}$ values remain constant within 2σ uncertainty (±3‰) over 220-km reconstructed distance. From 41 to 33 Ma, modeled paleoelevations ranged from 2,800 to 3,000 $^{+390}/_{-190}$ m in eastern Nevada, a region now at an average elevation of 1,500 m (Figure 2b). From 31 to 28 Ma, paleoelevations reached 2,400 $^{+300}/_{-250}$ m at 300–340-km inland in northeastern Nevada. From 27 to 23 Ma, peak paleoelevations increase to 3,400 $^{+370}/_{-270}$ m at 300–330-km inland, with the lowest δD_{glass} values measured from units in

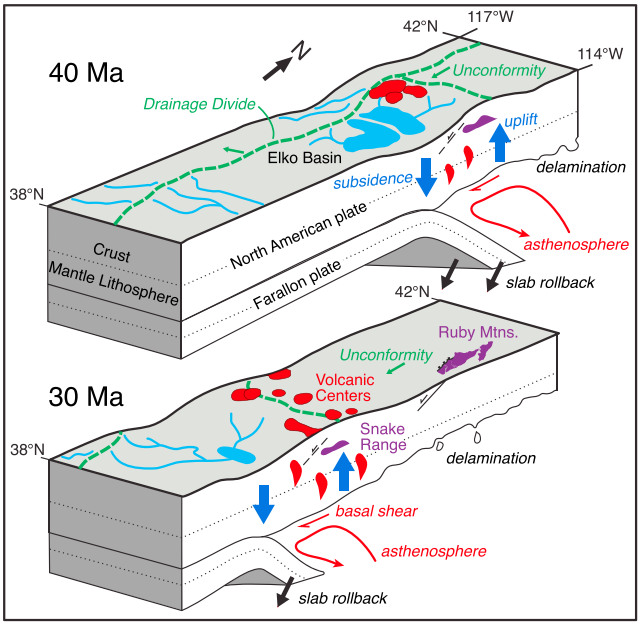

Figure 3. Interpretive lithosphere-scale perspective diagrams illustrating Farallon slab rollback processes at ca. 40 and 30 Ma in the central Cordilleran hinterland. Black arrows indicate direction of slab motion; blue arrows indicate subsidence from suction at the slab hinge and surface uplift from isostatic effects of heating and delamination. Red arrows show asthenospheric upwelling and basal shear from mantle flow. Incipient and exhumed metamorphic core complexes, normal faults, volcanism, erosion, and hydrology are also shown.

central Nevada. This is coincident with a prolonged absence of sediment accumulation in northeast Nevada (Best et al., 2016; Henry et al., 2012; Smith et al., 2017). Lower calculated paleoelevations for the early Oligocene relative to the Eocene are primarily an artifact of sample location differences. Early Oligocene samples at 338-km inland and the Eocene outlier value at 390 km ($\Delta\delta D_{glass}$ values = −40‰ to −50‰) were taken 130 and 180 km north, respectively, of the late Eocene samples at 356–415-km inland ($\Delta\delta D_{glass}$ values = −58‰ to −68‰; Figures 2 and S1). These differences in $\Delta\delta D_{glass}$ values likely reflect north-to-south topographic variability independent of transient drivers for surface uplift. The late Oligocene sample locations from >300-km inland ($\Delta\delta D_{glass}$ values = −70‰ to −90‰) span 150 km north-south (Figure S1), so their $\Delta\delta D$ values are comparable to both Eocene and early Oligocene samples. Peak modeled elevations in the hinterland during the Eocene and late Oligocene correlate with the paleodrainage divide determined using stratigraphic data (Figures 1 and S1; Cassel et al., 2014).

4. Landscape of the Hinterland Plateau

From 41 to 28 Ma, $\Delta\delta D_{glass}$ values do not change significantly (range: −55.4‰ to −62.4‰) for over 220-km paleo-distance from eastern Nevada to central Utah, with modeled elevations of 2.7–3.1 km (Figure 2). The lack of an inland δD value gradient indicates substantial moisture recycling in a hydrologically closed region (Brubaker et al., 1993), and, combined with the presence of multiple lacustrine basins (Figure 1), suggests that this was likely an internally drained plateau. Along much of the Cordilleran hinterland, regional stratigraphic trends demonstrate that lacustrine deposition on the plateau migrated southward over time, preceding rollback magmatism, and was followed by a depositional hiatus (Figure 3; Best et al., 2016; Gébelin et al., 2012; Henry et al., 2012; Smith et al., 2017). Thick packages of lacustrine strata contain sedimentary facies typical of the fluctuating profundal lacustrine facies association (Carroll & Bohacs, 1999), providing evidence for local subsidence and ponding of continental drainages (Figure 3). Interbedded ashes have enriched δD values signaling hydration by evaporated waters (Tables 1 and S1).

Instead of surface uplift, a regional decrease in δD_{glass} values like that observed at ca. 27 Ma could reflect the loss of evaporative moisture sources at the end of lacustrine deposition (e.g., Cassel et al., 2014; Ehlers & Poulsen, 2009), as moisture sourced from evaporative lake water would obscure the rainout effect (Dansgaard, 1964). Our new $^{40}Ar/^{39}Ar$ geochronology, however, shows that these lake strata were deposited between 49 and 34 Ma, and lacustrine sedimentary facies and enriched δD values are notably absent in younger strata (Smith et al., 2017). The new $^{40}Ar/^{39}Ar$ radioisotopic ages (Table 1) show that the regional decrease in δD_{glass} values occurred after 28 Ma, eliminating vapor recycling of evaporative lake waters as a possible source for the observed changes.

Modeling results show that a discrete surface uplift event totaling 400–600 $^{+390}/_{-270}$ m occurred in central Nevada by ca. 25 Ma, contemporaneous with migrating rollback volcanism. This modest total reflects the summed contributions from asthenospheric heating of hydrated lithosphere, isostatic unloading, and lithospheric delamination (Humphreys, 2009; Porter et al., 2017; Sternai et al., 2014; Figure 3). Based on these paleoelevations, previous crustal thickening would have accounted for 82–88% of measured late Oligocene topography. A high plateau reaching ~3 km in elevation extended eastward from the drainage divide to the edge of the Sevier thrust belt (Rocky Mountains) across Utah and eastern Nevada, similar to the Andean Altiplano. This plateau was likely a long-standing topographic feature. In addition to the high elevations from middle Eocene through Oligocene shown here, previous paleoaltimetry studies found relatively low δD values in minerals formed in and near the Snake Range and Raft River metamorphic core complexes (Figure 1), in comparison to known low foreland elevation samples from the Miocene, Eocene, and Cretaceous (Gébelin et al., 2012; Methner et al., 2015; Snell et al., 2014).

5. Implications for Slab Rollback Models

The record of surface deformation interpreted from these data requires previously thickened crust, surface uplift concurrent with or shortly following rollback magmatism, and modest overall surface uplift. The timing and magnitude of events are similar to recent models in which mantle flow, magmatic weakening, and delamination of rigid North American lithospheric mantle initiated or accelerated extension behind the arc (Brun et al., 2016; Chen et al., 2016; Porter et al., 2017; Sternai et al., 2014). Numerical models show that mantle flow generated by slab rollback contributes to surface deformation through changes to the thermal structure and buoyancy of the overlying lithosphere and the application of shear stresses to the base of the lithosphere or the crust (Figure 3; Chen et al., 2016; Menant et al., 2016; Sternai et al., 2014). Brun et al. (2016) concluded that rollback-driven mantle flow in the Aegean triggered the shift from localized core complex extension to distributed regional extension. Slab rollback processes across the Cordilleran hinterland may have promoted the propagation of the widespread crustal extension that led to the collapse of high topography and formed the characteristic topography of the Basin and Range province. Although several workers have inferred multiple kilometers of surface uplift to result from rollback and delamination in the hinterland (Chamberlain et al., 2012; Feng et al., 2013; Mix et al., 2011), our paleoelevations show that (1) high topography was preexisting across the Cordilleran hinterland of Utah and Nevada prior to and during slab removal, (2) hinterland extension prior to 23 Ma did not result in regional surface lowering, and (3) the magmatic weakening, lithospheric mantle delamination, and mantle flow shear stresses generated by slab rollback likely contributed to crustal extension and limited surface uplift to hundreds, not thousands, of meters.

Acknowledgments

NSF-EAR 1322073 supported this research. Full analytical data supporting the conclusions and additional sample processing details are available in the supporting information. We thank D. Breecker, T. Larson, D. Stockli, and B. Singer for laboratory support and C. Henry and A. Canada for field assistance. Reviews from A. Leier and A. Mulch greatly improved the manuscript. Cassel and Smith collected and processed samples, Cassel analyzed glass, Smith and Jicha analyzed sanidine, Cassel led writing efforts, and all authors contributed to the manuscript.

References

Armstrong, R. L., & Ward, P. (1991). Evolving geographic patterns of Cenozoic magmatism in the North American Cordillera: The temporal and spatial association of magmatic and metamorphic core complexes. *Journal of Geophysical Research*, *96*(B8), 13,201–13,224. https://doi.org/10.1029/91JB00412

Axelrod, D. I. (1997). Paleoelevation estimated from Tertiary floras. *International Geology Review*, *39*(12), 1124–1133. https://doi.org/10.1080/00206819709465319

Beerling, D. J., & Royer, D. L. (2011). Convergent Cenozoic CO_2 history. *Nature Geoscience*, *4*(7), 418–420. https://doi.org/10.1038/ngeo1186

Bendick, R., & Baldwin, J. (2009). Dynamic models for metamorphic core complex formation and scaling: The role of unchannelized collapse of thickened continental crust. *Tectonophysics*, *477*(1–2), 93–101. https://doi.org/10.1016/j.tecto.2009.03.017

Best, M. G., Christiansen, E. H., de Silva, S., & Lipman, P. W. (2016). Slab-rollback ignimbrite flareups in the southern Great Basin and other Cenozoic American arcs: A distinct style of arc volcanism. *Geosphere*, *12*(4), 1097–1135. https://doi.org/10.1130/ges01285.1

Brubaker, K. L., Entekhabi, D., & Eagleson, P. S. (1993). Estimation of continental precipitation recycling. *Journal of Climate*, *6*(6), 1077–1089. https://doi.org/10.1175/1520-0442

Brun, J.-P., Faccenna, C., Gueydan, F., Sokoutis, D., Philippon, M., Kydonakis, K., et al. (2016). The two-stage Aegean extension, from localized to distributed, a result of slab rollback acceleration. *Canadian Journal of Earth Sciences*, *53*(11), 1142–1157. https://doi.org/10.1139/cjes-2015-0203

Carroll, A. R., & Bohacs, K. M. (1999). Stratigraphic classification of ancient lakes: Balancing tectonic and climatic controls. *Geology*, *27*(2), 99–102. https://doi.org/10.1130/0091-7613(1999)027<0099:SCOALB>2.3.CO;2

Cassel, E. J., & Breecker, D. O. (2017). Long-term stability of hydrogen isotope ratios in hydrated volcanic glass. *Geochimica et Cosmochimica Acta*, *200*, 67–86. https://doi.org/10.1016/j.gca.2016.12.001

Cassel, E. J., Breecker, D. O., Henry, C. D., Larson, T. E., & Stockli, D. F. (2014). Profile of a paleo-orogen: High topography across the present-day Basin and Range from 40 to 23 Ma. *Geology*, *42*(11), 1007–1010. https://doi.org/10.1130/g35924.1

Chamberlain, C. P., Mix, H. T., Mulch, A., Hren, M. T., Kent-Corson, M. L., Davis, S. J., et al. (2012). The Cenozoic climatic and topographic evolution of the western North American Cordillera. *American Journal of Science*, *312*(2), 213–262. https://doi.org/10.2475/02.2012.05

Chen, Z., Schellart, W. P., Strak, V., & Duarte, J. C. (2016). Does subduction-induced mantle flow drive backarc extension? *Earth and Planetary Science Letters*, *441*, 200–210. https://doi.org/10.1016/j.epsl.2016.02.027

Colgan, J. P., & Henry, C. D. (2009). Rapid middle Miocene collapse of the Mesozoic orogenic plateau in north-central Nevada. *International Geology Review*, *51*(9–11), 920–961. https://doi.org/10.1080/00206810903056731

Coney, P. J., & Harms, T. A. (1984). Cordilleran metamorphic core complexes: Cenozoic extensional relics of Mesozoic compression. *Geology*, *12*(9), 550–554. https://doi.org/10.1130/0091-7613(1984)12<550:CMCCCE>2.0.CO;2

Constenius, K. N. (1996). Late Paleogene extensional collapse of the Cordilleran foreland fold and thrust belt. *Geological Society of America Bulletin*, *108*(1), 20–39. https://doi.org/10.1130/0016-7606(1996)108<0020:LPECOT>2.3.CO;2

Copeland, P., Currie, C. A., Lawton, T. F., & Murphy, M. A. (2017). Location, location, location: The variable lifespan of the Laramide orogeny. *Geology*, *45*(3), 223–226. https://doi.org/10.1130/G38810.1

Craig, H. (1961). Isotopic variations in meteoric waters. *Science*, *133*(3465), 1702–1703. https://doi.org/10.1126/science.133.3465.1702

Dallmeyer, R. D., Snoke, A., & McKee, E. H. (1986). The Mesozoic-Cenozoic Tectonothermal evolution of the Ruby Mountains, East Humboldt Range, Nevada: A Cordilleran metamorphic Core complex. *Tectonics*, *5*(6), 931–954. https://doi.org/10.1029/TC005i006p00931

Dansgaard, W. (1964). Stable isotopes in precipitation. *Tellus*, *16*, 436–468.

DeCelles, P. G. (2004). Late Jurassic to Eocene evolution of the Cordilleran thrust belt and foreland basin system, western U.S.A. *American Journal of Science*, *304*(2), 105–168. https://doi.org/10.2475/ajs.304.2.105

DeCelles, P. G., & Graham, S. A. (2015). Cyclical processes in the North American Cordilleran orogenic system. *Geology*, *43*(6), 499–502. https://doi.org/10.1130/G36482.1

Dickinson, W. R. (2009). Anatomy and global context of the North American Cordillera. In S. M. Kay, V. A. Ramos, & W. R. Dickinson (Eds.), *Backbone of the Americas: Shallow subduction, plateau uplift, and ridge and terrane collision*. *Geological Society of America Memoir, 204*, 1–29.

Doria, G., Royer, D. L., Wolfe, A. P., Fox, A., Westgate, J. A., & Beerling, D. J. (2011). Declining atmospheric CO_2 during the late Middle Eocene climate transition. *American Journal of Science*, *311*(1), 63–75. https://doi.org/10.2475/01.2011.03

Druschke, P., Hanson, A. D., Wells, M. L., Rasbury, T., Stockli, D. F., & Gehrels, G. (2009). Synconvergent surface-breaking normal faults of Late Cretaceous age within the Sevier hinterland, east-central Nevada. *Geology*, *37*(5), 447–450. https://doi.org/10.1130/g25546a.1

Ehlers, T., & Poulsen, C. J. (2009). Influence of Andean uplift on climate and paleoaltimetry estimates. *Earth and Planetary Science Letters*, *281*(3–4), 238–248. https://doi.org/10.1016/j.epsl.2009.02.026

Evans, S. L., Styron, R. H., van Soest, M. C., Hodges, K. V., & Hanson, A. D. (2015). Zircon and apatite (U-Th)/He evidence for Paleogene and Neogene extension in the Southern Snake Range, Nevada, USA. *Tectonics*, *34*, 2142–2164. https://doi.org/10.1002/2015TC003913

Feng, R., Poulsen, C. J., & Werner, M. (2016). Tropical circulation intensification and tectonic extension recorded by Neogene terrestrial $\delta^{18}O$ records of the western United States. *Geology*, *44*(11), 971–974. https://doi.org/10.1130/g38212.1

Feng, R., Poulsen, C. J., Werner, M., Chamberlain, C. P., Mix, H. T., & Mulch, A. (2013). Early Cenozoic evolution of topography, climate, and stable isotopes in precipitation in the North American Cordillera. *American Journal of Science*, *313*(7), 613–648. https://doi.org/10.2475/07.2013.01

Friedman, I., Gleason, J., Sheppard, R. A., & Gude, A. J. (1993). Deuterium fractionation as water diffuses into silicic volcanic ash. In P. K. Swart, K. C. Lohmann, J. McKenzie, & S. Savin (Eds.), *Climate change in continental isotopic records*, (Vol. 78, pp. 321–323). Washington, D.C.: American Geophysical Union.

Friedman, I., Smith, G. I., Johnson, C. A., & Moscati, R. J. (2002). Stable isotope compositions of waters in the Great Basin, United States 2. Modern precipitation. *Journal of Geophysical Research*, *107*(D19), 4401. https://doi.org/10.1029/2001JD000566

Gébelin, A., Mulch, A., Teyssier, C., Page Chamberlain, C., & Heizler, M. (2012). Coupled basin-detachment systems as paleoaltimetry archives of the western North American Cordillera. *Earth and Planetary Science Letters*, *335–336*, 36–47. https://doi.org/10.1016/j.epsl.2012.04.029

Gébelin, A., Teyssier, C., Heizler, M. T., & Mulch, A. (2015). Meteoric water circulation in a rolling-hinge detachment system (northern Snake Range core complex, Nevada). *Geological Society of America Bulletin*, *127*(1–2), 149–161. https://doi.org/10.1130/b31063.1

Gin, S., Jollivet, P., Fournier, M., Angeli, F., Frugier, P., & Charpentier, T. (2015). Origin and consequences of silicate glass passivation by surface layers. *Nature Communications*, *6*(1), 6360. https://doi.org/10.1038/ncomms7360

Heller, P. L., & Liu, L. (2016). Dynamic topography and vertical motion of the U.S. Rocky Mountain region prior to and during the Laramide orogeny. *Geological Society of America Bulletin*, *128*(5–6), 973–988. https://doi.org/10.1130/b31431.1

Henry, C. D., Hinz, N. H., Faulds, J. E., Colgan, J. P., John, D. A., Brooks, E. R., et al. (2012). Eocene-Early Miocene paleotopography of the Sierra Nevada-Great Basin-Nevadaplano based on widespread ash-flow tuffs and paleovalleys. *Geosphere*, *8*(1), 1–27. https://doi.org/10.1130/ges00727.1

Hodges, K. V., & Walker, J. D. (1992). Extension in the Cretaceous Sevier orogen, North American Cordillera. *Geological Society of America Bulletin*, *104*(5), 560–569. https://doi.org/10.1130/0016-7606(1992)104<0560:EITCSO>2.3.CO;2

Hren, M. T., Pagani, M., Erwin, D. M., & Brandon, M. (2010). Biomarker reconstruction of the early Eocene paleotopography and paleoclimate of the northern Sierra Nevada. *Geology*, *38*(1), 7–10. https://doi.org/10.1130/g30215.1

Humphreys, E. (2009). Relation of flat subduction to magmatism and deformation in the western United States. In S. M. Kay, V. A. Ramos, & W. R. Dickinson (Eds.), *Backbone of the Americas: Shallow Subduction, Plateau Uplift, and Ridge and Terrane Collision*. *Geological Society of America Memoir 204*, 85–98. https://doi.org/10.1130/2009.1204(04)

Ingraham, N. L., & Taylor, B. E. (1991). Light stable isotope systematics of large-scale hydrologic regimes in California and Nevada. *Water Resources Research*, *27*(1), 77–90. https://doi.org/10.1029/90WR01708

Jicha, B. R., Singer, B. S., & Sobol, P. (2016). Re-evaluation of the ages of $^{40}Ar/^{39}Ar$ sanidine standards and supereruptions in the western U.S. using a Noblesse multi-collector mass spectrometer. *Chemical Geology*, *431*, 54–66. https://doi.org/10.1016/j.chemgeo.2016.03.024

Kendall, C., & Coplen, T. B. (2001). Distribution of oxygen-18 and deuterium in river waters across the United States. *Hydrological Processes*, *15*(7), 1363–1393. https://doi.org/10.1002/hyp.217

Konstantinou, A., Strickland, A., Miller, E. L., & Wooden, J. P. (2012). Multistage Cenozoic extension of the Albion—Raft River—Grouse Creek metamorphic core complex: Geochronologic and stratigraphic constraints. *Geosphere*, *8*(6), 1429–1466. https://doi.org/10.1130/ges00778.1

Kuiper, K. F., Deino, A., Hilgen, F. J., Krijgsman, W., Renne, P. R., & Wijbrans, J. R. (2008). Synchonizing rock clocks of Earth history. *Science*, *320*(5875), 500–504. https://doi.org/10.1126/science.1154339

Lee, J.-Y., Marti, K., Severinghaus, J. P., Kawamura, K., Yoo, H.-S., Lee, J.-B., & et al. (2006). A redetermination of the isotopic abundances of atmospheric Ar. *Geochimica et Cosmochimica Acta*, *70*(17), 4507–4512. https://doi.org/10.1016/j.gca.2006.06.1563

Liu, M. (2001). Cenozoic extension and magmatism in the North American Cordillera: The role of gravitational collapse. *Tectonophysics*, *342*(3–4), 407–433. https://doi.org/10.1016/S0040-1951(01)00173-1

Liu, Z., Pagani, M., Zinniker, D., DeConto, R., Huber, M., Brinkhuis, H., et al. (2009). Global cooling during the Eocene-Oligocene climate transition. *Science*, *323*(5918), 1187–1190. https://doi.org/10.1126/science.1166368

Long, S. P. (2012). Magnitudes and spatial patterns of erosional exhumation in the Sevier hinterland, eastern Nevada and western Utah, USA: Insights from a Paleogene paleogeographic map. *Geosphere*, *8*(4), 881–901. https://doi.org/10.1130/GES00783.1

Long, S. P., Thomson, S. N., Reiners, P. W., & Di Fiori, R. V. (2015). Synorogenic extension localized by upper-crustal thickening: An example from the Late Cretaceous Nevadaplano. *Geology*, *43*(4), 351–354. https://doi.org/10.1130/g36431.1

Lund Snee, J. E., Miller, E. L., Grove, M., Hourigan, J. K., & Konstantinou, A. (2016). Cenozoic paleogeographic evolution of the Elko Basin and surrounding region, northeast Nevada. *Geosphere*, *12*(2), 464–500. https://doi.org/10.1130/ges01198.1

McGrew, A. J., & Snee, L. W. (1994). $^{40}Ar/^{39}Ar$ thermochronologic constraints on the tectonothermal evolution of the northern East Humboldt Range metamorphic core complex, Nevada. *Tectonophysics*, *238*(1–4), 425–450. https://doi.org/10.1016/0040-1951(94)90067-1

Menant, A., Sternai, P., Jolivet, L., Guillou-Frottier, L., & Gerya, T. (2016). 3D numerical modeling of mantle flow, crustal dynamics and magma genesis associated with slab roll-back and tearing: The eastern Mediterranean case. *Earth and Planetary Science Letters*, *442*, 93–107. https://doi.org/10.1016/j.epsl.2016.03.002

Methner, K., Mulch, A., Teyssier, C., Wells, M. L., Cosca, M. A., Gottardi, R., et al. (2015). Eocene and Miocene extension, meteoric fluid infiltration, and core complex formation in the Great Basin (Raft River Mountains, Utah). *Tectonics*, *34*, 680–693. https://doi.org/10.1002/2014tc003766

Min, K., Mundil, R., Renne, P. R., & Ludwig, K. R. (2000). A test for systematic errors in $^{40}Ar/^{39}Ar$ geochronology through comparison with U-Pb analysis of a 1.1 Ga rhyolite. *Geochimica et Cosmochimica Acta*, *64*(1), 73–98. https://doi.org/10.1016/S0016-7037(99)00204-5

Mix, H. T., Ibarra, D. E., Mulch, A., Graham, S. A., & Chamberlain, C. P. (2016). A hot and high Eocene Sierra Nevada. *Geological Society of America Bulletin*, *128*(3–4), 531–542. https://doi.org/10.1130/b31294.1

Mix, H. T., Mulch, A., Kent-Corson, M. L., & Chamberlain, C. P. (2011). Cenozoic migration of topography in the North American Cordillera. *Geology*, *39*(1), 87–90. https://doi.org/10.1130/g31450.1

Mulch, A., Graham, S. A., & Chamberlain, C. P. (2006). Hydrogen isotopes in Eocene river gravels and paleoelevation of the Sierra Nevada. *Science*, *313*(5783), 87–89. https://doi.org/10.1126/science.1125986

Mulch, A., Teyssier, C., Cosca, M. A., & Chamberlain, C. P. (2007). Stable isotope paleoaltimetry of Eocene core complexes in the North American Cordillera. *Tectonics*, *26*, TC4001. https://doi.org/10.1029/2006tc001995

Pearson, P. N., Foster, G. L., & Wade, B. S. (2009). Atmospheric carbon dioxide through the Eocene-Oligocene climate transition. *Nature*, *461*(7267), 1110–1113. https://doi.org/10.1038/nature08447

Porter, R., Hoisch, T., & Holt, W. E. (2017). The role of lower-crustal hydration in the tectonic evolution of the Colorado Plateau. *Tectonophysics*, *712–713*, 221–231. https://doi.org/10.1016/j.tecto.2017.05.025

Poulsen, C. J., & Jeffery, M. L. (2011). Climate change imprinting on stable isotopic compositions of high-elevation meteoric water cloaks past surface elevations of major orogens. *Geology*, *39*(6), 595–598. https://doi.org/10.1130/g32052.1

Rey, P. F., Teyssier, C., & Whitney, D. L. (2009a). Extension rates, crustal melting, and core complex dynamics. *Geology*, *37*(5), 391–394. https://doi.org/10.1130/g25460a.1

Rey, P. F., Teyssier, C., & Whitney, D. L. (2009b). The role of partial melting and extensional strain rates in the development of metamorphic core complexes. *Tectonophysics*, *477*(3–4), 135–144. https://doi.org/10.1016/j.tecto.2009.03.010

Rowley, D. B. (2007). Stable isotope-based paleoaltimetry: Theory and validation. *Reviews in Mineralogy and Geochemistry*, *66*(1), 23–52. https://doi.org/10.2138/rmg.2007.66.2

Sheldon, N. D., Grimes, S. T., Hooker, J. J., Collinson, M. E., Bugler, M. J., Hren, M. T., et al. (2016). Coupling of marine and continental oxygen isotope records during the Eocene-Oligocene transition. *Geological Society of America Bulletin*, *128*(3–4), 502–510. https://doi.org/10.1130/b31315.1

Smith, M. E., Carroll, A. R., Jicha, B. R., Cassel, E. J., & Scott, J. J. (2014). Paleogeographic record of Eocene Farallon slab rollback beneath western North America. *Geology*, *42*(12), 1039–1042. https://doi.org/10.1130/G36025.1

Smith, M. E., Cassel, E. J., Jicha, B. R., Singer, B. S., & Canada, A. S. (2017). Hinterland drainage closure and lake formation in response to middle Eocene Farallon slab removal, Nevada, U.S.A. *Earth and Planetary Science Letters*, *479*, 156–169. https://doi.org/10.1016/j.epsl.2017.09.023

Snell, K. E., Koch, P. L., Druschke, P., Foreman, B. Z., & Eiler, J. M. (2014). High elevation of the 'Nevadaplano' during the Late Cretaceous. *Earth and Planetary Science Letters*, *386*, 52–63. https://doi.org/10.1016/j.epsl.2013.10.046

Sonder, L. J., & Jones, C. H. (1999). Western United States Extension: How the west was widened. *Annual Review of Earth and Planetary Sciences*, *27*(1), 417–462. https://doi.org/10.1146/annurev.earth.27.1.417

Stauffer, E. (2017). Volcanic glass as a meteoric water proxy: Determining hydrogen isotope fractionation from the Mazama Ash in Western North America. (B.S. Senior Thesis), University of Idaho, University of Idaho Libraries.

Sternai, P., Jolivet, L., Menant, A., & Gerya, T. (2014). Driving the upper plate surface deformation by slab rollback and mantle flow. *Earth and Planetary Science Letters*, *405*, 110–118. https://doi.org/10.1016/j.epsl.2014.08.023

Wells, M. L., Hoisch, T. D., Cruz-Uribe, A. M., & Vervoort, J. D. (2012). Geodynamics of synconvergent extension and tectonic mode switching: Constraints from the Sevier-Laramide orogen. *Tectonics*, *31*, TC4015. https://doi.org/10.1029/2011tc002913

Whitney, D. L., Teyssier, C., Rey, P., & Buck, W. R. (2013). Continental and oceanic core complexes. *Geological Society of America Bulletin*, *125*(3–4), 273–298. https://doi.org/10.1130/b30754.1

Wolfe, J. A., Forest, C. E., & Molnar, P. (1998). Paleobotanical evidence of Eocene and Oligocene paleoaltitudes in midlatitude western North America. *Geological Society of America Bulletin*, *110*(5), 664–678. https://doi.org/10.1130/0016-7606(1998)110<0664:PEOEAO>2.3.CO;2

Xia, Z.-h., Xu, B.-q., Mügler, I., Wu, G.-j., Gleixner, G., Sachse, D., & et al. (2008). Hydrogen isotope ratios of terrigenous *n*-alkanes in lacustrine surface sediment of the Tibetan Plateau record the precipitation signal. *Geochemical Journal*, *42*(4), 331–338. https://doi.org/10.2343/geochemj.42.331